

High-Efficiency Hexagonal Nanowire MAPbI_3 Perovskite Solar Cell with Broadband Light Trapping

Kawshik Nath^{a,b}, Bibekananda Nath^{a,b} and Ahmed Zubair^{a,*}

^a Department of Electrical and Electronic Engineering, Bangladesh University of Engineering and Technology, Dhaka, Bangladesh

^b Department of Electrical and Electronic Engineering, Chittagong University of Engineering and Technology, Chattogram, Bangladesh

ARTICLE INFO

Keywords:

Photovoltaics
Hexagonal Nanowire
Perovskite Solar Cell
Finite Difference Time Domain
Polarization Insensitive
Transverse Electric and Transverse Magnetic

ABSTRACT

Perovskite solar cells (PSCs) have emerged as strong contenders for the next generation of photovoltaic (PV) technologies due to their exceptional light absorption properties, tunability, and affordability in manufacturing. Here, we presented an ingenious hexagonal nanowire (HNW)-based PSC that achieves broadband absorption, minimizes reflectance, and offers robust polarization insensitivity by improving light-matter interaction and increasing charge-collection efficiency. The rotational symmetry of the HNW configuration yielded polarization-independent absorbance under both TE and TM illumination across the visible and near-infrared spectra. The optimization of the geometrical parameters of $\text{CH}_3\text{NH}_3\text{PbI}_3$ -based HNW structure, including diameter, period, and fill ratio, offered a wide range of variations that influenced both optical properties and device performance. To further intensify photon confinement, a dielectric SiO_2 sphere is partially embedded in the ITO layer, improving long-wavelength absorbance and increasing electron-hole pair generation near the active region. We analyzed the finite-difference time-domain (FDTD) method to examine the optical properties of our proposed structure. This study demonstrates that our proposed structure has achieved a higher generation rate, enhanced absorbance, and a higher optical short-circuit current density (J_{sc}) of 29.53 mA/cm^2 . Electrical performance is assessed by solving the coupled drift-diffusion and Poisson equations for the dynamics of carrier transport. The optimized HNW structure achieved a notable power conversion efficiency of 24.2%, highlighting a strong connection between optical confinement and effective carrier transport. These attributes render the proposed HNW PSC a viable option for high-performance PV systems and scalable thin-film solar technologies.

1. Introduction

To address the escalating energy demands of the 21st century, solar cell technologies have been increasingly directed toward the efficient generation of renewable solar power, demonstrating rapid and sustained growth in recent years [1, 2, 3, 4]. Among the various photovoltaic (PV) technologies, perovskite solar cells (PSCs) have emerged as leading contenders due to their tunable bandgaps, extended carrier diffusion lengths, enhanced charge transport properties, and straightforward fabrication processes. Besides, PSCs have rapidly gained recognition as one of the most promising PV technologies, offering the potential for high efficiency at reduced production costs [5, 6, 7]. Among different organic materials, MAPbI_3 has been widely adopted in PSCs since its initial introduction by Kojima *et al.* in 2009 [8]. Furthermore, comprehensive studies demonstrated that lead (Pb)-based PSCs exhibit superior power conversion efficiencies (PCEs) compared to their lead-free counterparts [9, 10, 11]. Both industrial and academic communities have shown significant interest in the emerging technology of lead (Pb) halide PSCs, particularly due to their remarkable advancements in PCEs, which surpassed 23 % [12]. Additionally, the open-circuit voltages (V_{oc}) of perovskite devices are approaching the theoretical radiative limit, for instance,

1.32 V of V_{oc} was reported for MAPbI_3 [13, 14, 15], given its bandgap ($E_g \approx 1.6 \text{ eV}$) [16]. The majority of solar cell architectures employ either mesoporous or planar configurations, incorporating a perovskite absorber layer sandwiched between the hole-transport layer (HTL) and the electron-transport layer (ETL).

Recently, Wang *et al.* developed $\text{TiO}_2/\text{MAPbI}_3/\text{NiO}$ PSCs with TiO_2 nanowire (NW) ETL arrays and reported a PV conversion efficiency of 21.8% [17]. Hmaidi *et al.* proposed Si NW as HTL for MAPbI_3 perovskite material and found 11.93% efficiency [18]. To improve the absorbance range (200-2500 nm) and eventually the efficiency of the PSC, Ren *et al.* combined quantum dots (QDs) with perovskite material and created an ETL/QD/perovskite layer/HTL core-shell structure NW array solar cell [19]. Moreover, Liang *et al.* designed an Ag NW-based MAPbI_3 PSC to achieve tunable transmittance, reporting a maximum efficiency of 17.3% [20]. To further enhance performance, they designed a homojunction p-type MAPbI_3 /n-type MAPbI_3 solar cell to reduce the generated carriers' recombination by creating an internal electric field, and they achieved an efficiency of 22% for a certain thickness of the absorber layer [21]. To push the PCE beyond 25%, recent research efforts have focused on advanced architectures such as bifacial 3D/3D, 3D/2D, or even multi-stacked perovskite layers. Alathlwi *et al.* proposed a PET/Ag NWs: MXenes/ SrCuO_2 /(FAPbI₃)_{0.95}(MAPbBr₃)_{0.05}/C₆₀/BCP/FTO solar cell structure, achieving a high PCE of approximately 26% [22]. Mkwai *et al.* fabricated a GeS-doped MAPbI_3 solar cell and reported an efficiency of 17.46% [23]. However,

*Corresponding author

 ahmedzubair@eee.buet.ac.bd (A. Zubair)

 <http://ahmedzubair.buet.ac.bd/> (A. Zubair)

ORCID(s): 0009-0001-9749-278X (K. Nath); 0009-0000-2213-6628 (B. Nath); 0000-0002-1833-2244 (A. Zubair)

2D/3D structures primarily suffer from high series resistance and poor charge transport efficiency due to unmatched lattice parameters and non-symmetrical conductivity. To overcome such issues, Patil *et al.* proposed a 3D/3D bilayer MAPbI₃/FAPbI₃ heterojunction solar cell and obtained an PCE of 23.08% [24]. However, these types of multilayer structures are both costly and complex to fabricate. To overcome such issues, several studies have developed monolayer perovskite absorbers of various shapes. Im *et al.* fabricated NW-shaped MAPbI₃ through the two-step spin-coating procedure and reported an efficiency of 14.71% under standard AM 1.5G solar irradiation [25]. Sing *et al.* further improved the efficiency of the NW perovskite to 18.7% by adding fullerene derivative (PC₆₀BM) [26]. To eradicate the ionic defects at the grain boundary and from the surface to improve the efficiency of organic-inorganic PSCs, Cha *et al.* demonstrated a nanowire hybrid PSC (NWPSC) and charge transport layers with an efficiency of 21.56% and stability up to 3500 hours [27]. Despite significant advancements in PSCs utilizing multilayer heterostructures, 2D/3D junctions, and nanowire morphologies, these configurations often encounter issues such as polarization-dependent optical responses, inefficient electromagnetic field localization, and the need for additional transport layers. Moreover, conventional NW architectures generally enhance absorbance via localized resonances but lack geometrical symmetry, resulting in a nonuniform field localization and minimal carrier extraction. Moreover, the inefficient field localization hinders the capability of broadband absorption under the unpolarized illumination. There is a scope for research to design structures that mitigate these limitations by enhancing light-matter interaction, near-field confinement, and efficient carrier extraction within a single absorber framework [28].

In this work, we conducted a comprehensive optoelectronic study of an Hexagonal Nanowire (HNW)-based CH₃NH₃PbI₃ (MAPbI₃) PSC aimed at achieving efficient light trapping by employing physical mechanisms governed by the light matter interaction and the carrier dynamics. We investigated the optical and electrical performance of the proposed structure using the finite-difference time-domain (FDTD) method, coupled with a self-consistent solution of drift-diffusion and the Poisson equation for the transverse electric (TE), transverse magnetic (TM), and unpolarized light [29]. Our findings indicated that the HNW design facilitates a significant enhancement in broadband absorption and effective charge extraction. It showed behavior that is independent of polarization by enhancing the near-field confinement. Additionally, an analysis of the generation rate profile and electric field distributions revealed the influence of the hexagonal architecture in directing and localizing light, which in turn enhanced carrier generation and the overall PV performance. The electrical simulations demonstrated a high PCE attributed to the broadband light absorbance throughout our proposed structure and exhibited superior performance compared to the recently developed MAPbI₃ based PSCs of various configurations. Alongside the numerical analysis, this study addresses the practical

challenges of experimentally realizing the structures to enable their commercial utilization.

2. Structure Design and Simulation Methodology

2.1. Structural Design

The proposed structure consists of an HNW-based PSC as shown in Fig. 1 (a). The design includes a vertically aligned HNW made of MAPbI₃ perovskite material. To improve the light confinement and scattering along the absorber region, a SiO₂ based sphere is introduced in two different configurations: one placed on top of the indium-doped tin oxide (ITO) layer and another one partially embedded inside it according to Figs. 1 (b), and (c). This configuration allows for Mie resonance and enhanced light confinement. The optimal thickness of each layer is also given in this figure. Here, the dielectric sphere acts as an optical concentrator, directing the incident photons into the perovskite layer by enhancing light coupling, promoting scattering, and minimizing reflectance losses. The ITO layer simultaneously allows for high optical transmittance and efficient lateral charge transport while exhibiting negligible parasitic absorbance across the visible spectral range. The ETL made of TiO₂ allows for the selective extraction of electrons from the photoactive perovskite layer and guides the electrons toward the metal contact, effectively preventing hole recombination through proper energy band alignment. Conversely, HTL made of spiro-OMeTAD promotes the efficient collection of generated holes while also serving as an electronic barrier to prevent unwanted electron backflow, thus ensuring strong charge carrier selectivity. The rear metal contact enables the removal of stored charge carriers and completes the PV circuit with minimal resistive and optical losses. In this study, we used aluminum (Al) as a back contact.

2.2. Simulation Methodology

We conducted optical simulations of the proposed structure utilizing the three-dimensional FDTD method using *Ansys Lumerical* [29]. Due to the periodicity of the structure along the x and y axes, we performed the simulation over a unit cell and applied periodic boundary conditions in both directions. To reduce unwanted reflectances along the z axis, we incorporated 64 perfectly matched layers (PMLs) on both the top and bottom of the model. We chose a non-uniform mesh with a step size of 0.25 nm, and also incorporated an override mesh for each layer to ensure better accuracy. Mesh refinement was performed by implementing the integral solution of Maxwell's equations near the interface for all the materials, including metals, which can lead to better convergence and accuracy.

We utilized a downward-directed continuous wave (CW) normalized plane wave source, spanning wavelengths from 300 to 850 nm, to analyze the performance of our designed perovskite cell for TM, TE, and unpolarized incident waves. To determine the optical performance, frequency-domain field and power monitors were employed to enumerate the

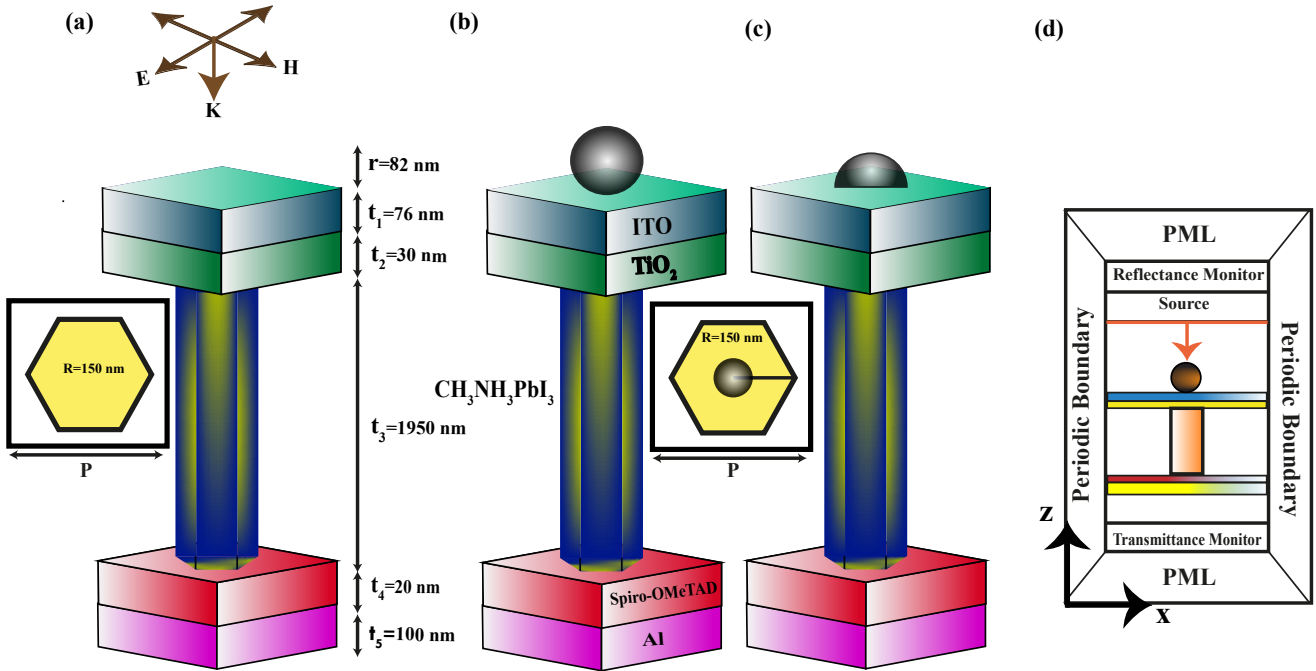


Figure 1: (a) Schematics of the unit cell of an HNW-based nanostructured PSC, (b) including a SiO_2 based sphere on top of the ITO, (c) inserting the sphere inside the ITO , (d) cross-sectional view of the xz plane of our proposed structure with simulation setup.

transmitted and reflected light passing through the photoactive layer. These monitors captured the characteristics of transmittance, $T(\lambda)$, and reflectance, $R(\lambda)$, spectra as a function of wavelength. The simulation environment is illustrated in Fig. 1 (d). To achieve accurate optical simulations, the refractive index (n) and extinction coefficient (k) for all materials were carefully incorporated into the model. The dispersive optical properties for Al and SiO_2 were collected from Palik *et al.* [30] and for TiO_2 , Spiro-OMeTAD, and MAPbI_3 were gathered from Elewa *et al* [31].

The transmittance and reflectance spectra are calculated by,

$$R(\lambda) = \frac{P_R}{P_I}, \quad (1)$$

$$T(\lambda) = \frac{P_T}{P_I}. \quad (2)$$

Here, P_I , P_R , and P_T indicate the incident, reflected, and transmitted wave's power, respectively. The absorbance, $A(\lambda)$ is wavelength-dependent and can be determined by,

$$A(\lambda) = 1 - (R(\lambda) + T(\lambda)). \quad (3)$$

The electrical performance parameters of the proposed PSC were determined by using Poisson's and drift-diffusion equations as follows:

$$J_n = q\mu_n n E + qD_n \nabla n, \quad (4)$$

$$J_p = q\mu_p p E - qD_p \nabla p. \quad (5)$$

Here, J_n and J_p indicate the current densities of electrons and holes, respectively, measured in mA cm^{-2} . The parameter q stands for the charge of an electron, while μ_n and μ_p refer to the mobilities of electrons and holes. The electric field is represented by E , and D_n and D_p denote the diffusion constants of electrons and holes, respectively. The concentrations of charge carriers for electrons and holes are represented by n and p , respectively. The characteristics of these charge carriers are determined by two main mechanisms: drift, which is affected by an external electric field, and diffusion, which occurs due to concentration differences driven by thermal energy. Carrier mobility (μ_p) quantifies the speed at which electrons or holes move through a semiconductor when an electric field is present. It is a crucial factor in assessing the efficiency of charge transport. This mobility is also thermodynamically connected to the diffusivities D_n and D_p through the Einstein relation, which is given by,

$$D_{n(p)} = \mu_{n(p)} \frac{k_B T_{abs}}{q} \quad (6)$$

Here, k_B represents the Boltzmann constant, T_{abs} denotes the absolute temperature, and q indicates the charge of the carriers. This relationship provides a theoretical basis that links the random thermal motion of carriers (diffusion) with their directed movement under an electric field (drift), thereby connecting microscopic thermal dynamics to the

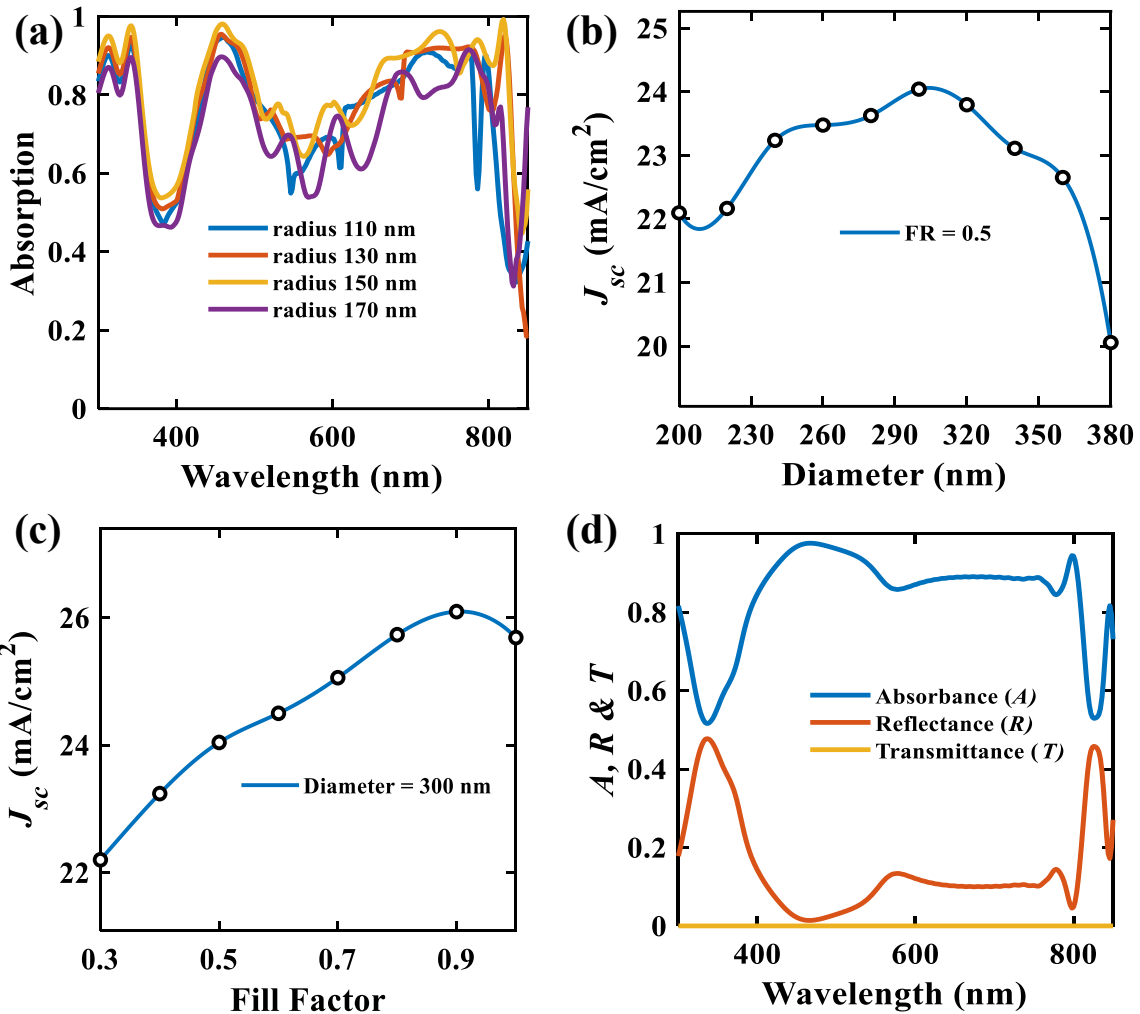


Figure 2: (a) Absorbance spectra for different radius at a fixed FR of 0.5, (b) optical J_{sc} for different radius at FR = 0.5, (c) optical J_{sc} for a fixed radius of 150 nm for varying FR, (d) absorbance, reflectance, and transmittance spectra for FR = 0.9 at a radius of 150 nm.

macroscopic electrical properties of semiconducting materials. The Shockley–Read–Hall (SRH) mechanism is the major non-radiative recombination process, which significantly limits the efficiency of PSCs. As a result, the kinetics of carrier recombination in the perovskite absorber layer are analyzed quantitatively using the expression for the SRH recombination rate.

$$R_{SRH} = \frac{np - n_i^2}{\tau_n(n + n_i) + \tau_p(p + n_i)} \quad (7)$$

Here, τ_n , τ_p , and n_i are the lifetimes of the electron and the hole, and the intrinsic carrier concentration, respectively.

The total number of photons absorbed can be calculated by taking the absorbance profile P_{abs} and dividing it by the energy corresponding to a single photon, represented by the following equation:

$$G = \frac{P_{abs}}{\hbar\nu} \quad (8)$$

Here, \hbar stands for the reduced Planck's constant and ν is the frequency of light. The generation rate G is derived by

integrating this photon flux across the relevant wavelength or frequency range within the simulated spectrum.

Assuming unit internal quantum efficiency, the resulting photogeneration current I_p can be approximated as equation 9 by considering each absorbed photon results in the generation of an electron–hole pair:

$$I_p = eG \quad (9)$$

The quantum efficiency $QE(\lambda)$ of a solar cell can be expressed by,

$$QE(\lambda) = \frac{P_{abs}(\lambda)}{P_{in}(\lambda)} \quad (10)$$

Here, $P_{in}(\lambda)$ and $P_{abs}(\lambda)$ represent the incident and absorbed radiative powers into the PSC at a particular wavelength λ , respectively.

The impact of geometric features, such as size and shape, on device performance was then evaluated by analyzing power–voltage (P–V) and current density–voltage (J–V)

characteristics. The short-circuit current density (J_{sc}) was calculated by the following equation:

$$J_{sc} = \frac{q}{\hbar c} \int_{300 \text{ nm}}^{850 \text{ nm}} \text{EQE}(\lambda) \lambda I_{\text{AM1.5}}(\lambda) d\lambda \quad (11)$$

Here, c refers to the speed of light. The upper limit of the integration corresponds to the wavelength determined by the bandgap of the perovskite material, which prevents absorbance below this energy threshold, as absorbance of photons below this will not contribute to electron-hole pair generation.

The PCE is another important metric used to examine the electrical performance of solar cells and is defined by,

$$\eta = \frac{\text{FF} \cdot V_{oc} \cdot J_{sc}}{P_{\text{AM1.5G}}}. \quad (12)$$

$P_{\text{AM1.5G}}$ represents the incident solar power density from the AM1.5G spectrum, usually taken as 100 mW/cm².

3. Results and Discussion

3.1. Optical Analysis

3.1.1. Geometric Optimization for Light Management in HNW

The optical properties of HNW solar cells are significantly influenced by their geometric parameters, including diameter (D), period (P), and the fill ratio (FR), which can be defined as D/P . The objective of the optical simulation was primarily to maximize the photocurrent generated by absorbed photons, which also relies on the geometric parameters of the nanostructures. Fig. 2(a) depicts the absorbance spectra for different NW diameters (D) maintained at a constant fill ratio ($FR = 0.5$). As the radius ($R = D/2$) decreases from 110 nm to 150 nm, the absorbance characteristics become broader and more uniform in the 450-800 nm spectrum. This improvement stems from enhanced light confinement, increased photonic coupling, and longer effective optical paths within the perovskite NW, leading to higher photon absorbance. The peak optical J_{sc} of 24.01 mA/cm² is observed at $R = 150$ nm, from Fig. 2(b). At $R = 170$ nm, the absorbance curve experiences a decline, especially in the 600-800 nm range, where longer-wavelength photons are not efficiently captured. Due to the more efficient excitation and confinement of the photons inside the NW, HNWs with a diameter of 300 nm demonstrated significantly better optical absorbance [25]. Therefore, further increasing the NWs radius beyond 150 nm degrades the absorbance, as can be observed from Fig. 2(a).

After the optimized diameter for HNW was determined, the periodicity of the NW needs to be optimized to achieve the most efficient and well-structured design. To achieve this, NW's with a constant radius of 150 nm were simulated at various FR s ranging from 0.3 to 1.0. In Fig. 2(c), the photon-generated current density is shown for a fixed radius. Due to the inverse relationship between the FR and P , a lower FR corresponds to a wider interwire spacing.

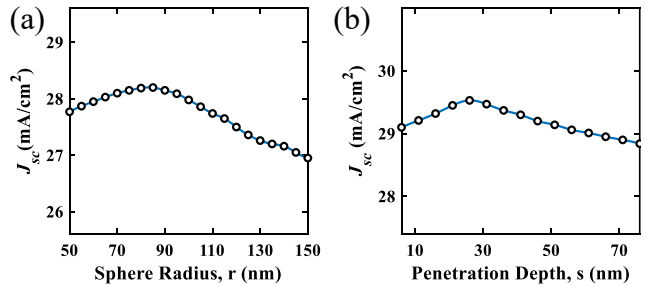


Figure 3: Optical J_{sc} values (a) SiO_2 sphere on ITO layer, (b) SiO_2 sphere partially embedded into the ITO layer.

Structures with $FR < 0.5$ exhibit inadequate absorbance, attributed to weaker field localization and reduced optical confinement, as indicated by the simulation results. Conversely, FR values in the range of 0.7 to 0.9 demonstrate improved J_{sc} and enhanced light absorbance, indicating a more favorable photonic coupling. The optimum configuration yields a peak optical J_{sc} of 26.09 mA/cm², corresponding to a NW diameter of 300 nm and an FR of 0.9. This optimized structure represents a well-balanced design that maximizes both carrier generation and light-matter interaction in the HNW array. Subsequently, for this proposed configuration, the ETL and HTL layers were optimized, resulting in a peak optical J_{sc} of 27.02 mA/cm². Fig. 2(d) represents the absorbance, reflectance, and transmittance spectra for the fill ratio of 0.9 and a diameter of 300 nm. From this figure, the absorbance curve (blue) indicates consistently high values greater than 85% throughout most of the visible spectrum, particularly between 450 and 780 nm, which reveals an outstanding ability to harvest light. The high level of absorbance is due to the strong interaction between light and matter, facilitated by the hexagonal structure, which improves optical confinement. From the transmittance spectra, it can be seen that the transmittance is nearly zero, which means most of the light is absorbed by the structure and a small portion is reflected.

To further enhance light confinement and improve device performance beyond the optimized HNW configuration, we performed a radius-dependent optimization study by incorporating a dielectric SiO_2 sphere on top of the ITO layer. The SiO_2 sphere was introduced with two primary objectives. First, it promotes stronger light trapping by encouraging constructive interference and enhancing the coupling of incoming photons due to the enhanced field localization of the HNW array. Second, it introduces negligible parasitic absorbance in the operating wavelength range [32]. From this analysis, we achieved the maximum optical J_{sc} of 28.2 mA/cm² at a radius (r) of 82 nm identified a r of 82 nm as demonstrated in Fig. 3 (a). Guided by this result, the optimized SiO_2 sphere was subsequently integrated into the structure, allowing it to partially penetrate the ITO layer and enabling the effective redirection and redistribution of incoming light into the perovskite NW region. This design modification scatters and redirects incoming light into the active region, thereby increasing the

Table 1
Electrical properties of the materials used in this simulation

Property	MAPbI ₃ (Perovskite)	TiO ₂ (ETL)	Spiro-OMeTAD (HTL)
DC Permittivity, ϵ	6.25	7.84	7.5
Work Function (eV)	4.68	5.6	3.655
E_c Valley	X	X	X
Effective mass, m_n ($1/m_e$)	4.63	11.67	4.63
Effective mass, m_p ($1/m_e$)	4.63	3.99	4.63
Bandgap, E_g (eV)	1.5	3.2	2.91
Acceptor doping, N_A (cm^{-3})	2.4×10^{17}	—	3×10^{18}
Donor doping, N_D (cm^{-3})	—	5×10^{19}	—
Electron mobility, μ_n (cm^2/Vs)	50	0.006	0.0001
Hole mobility, μ_p (cm^2/Vs)	50	0.006	0.0001
Auger Recombination coefficient for electron, C_n (cm^6/s)	2.7×10^{-29}	—	—
Auger Recombination coefficient for hole, C_p (cm^6/s)	4.6×10^{-29}	—	—
Trap Assisted Recombination coefficient for electron, τ_n (ns)	8	5	5
Trap Assisted Recombination coefficient for hole, τ_p (ns)	8	5	2

optical path length within the nanostructured absorber. Consequently, the addition of the sphere mitigates the reduced absorbance observed at higher filling ratios and results in improved broadband absorption and an increased optical J_{sc} of 29.53 mA/cm² as depicted in Fig. 3 (b). Here, we considered the penetration depth as 's' in nm.

This improvement is further validated by Fig. 4(a), which represents the absorbance spectra for three different configurations: (i) HNW structure without SiO₂ sphere, (ii) SiO₂ sphere on ITO layer, and (iii) SiO₂ sphere partially embedded inside ITO layer. The figure shows that when the SiO₂ sphere is embedded within the ITO layer, absorbance exceeding 90% is sustained across the 400–800 nm wavelength range. Fig. 4(b) shows the simulated spectra for absorbance (A), reflectance (R), and transmittance (T) of the optimized HNW PSC when the SiO₂ sphere is in the ITO layer. Two distinct absorbance peaks are observed. A notable increase in absorbance around 430 nm to 650 nm is linked to the coupling of high-energy photons via pronounced interface-induced field localization between successive layers. A second significant peak in the range of 830–850 nm is probably due to the Fabry-Pérot (FP) type interference occurring at longer wavelengths. The high level of absorbance is attributed to the improvement of optical confinement and effective coupling of incoming light into Mie-resonant and FP-cavities present within the absorber.

In order to provide a more comprehensive physical understanding of the observed absorbance features, we utilized analytical expressions derived from classical electrodynamics and Mie scattering theory, which demonstrate how the sphere enhances the light matter interaction into the absorber layer [33, 34]. The fundamental descriptor governing the sphere–light interaction is the Mie size parameter,

$$x = \frac{2\pi r}{\lambda}, \quad (13)$$

which determines the shift between Rayleigh ($x \ll 1$), Mie ($x \sim 1$), and geometric-optics ($x \gg 1$) regimes. For the optimized sphere radius of $r = 82$ nm, the size

parameter varies from $x = 0.60$ to 1.47 over the operating wavelength range (350–850 nm), placing the structure firmly in the resonant Mie-scattering regime where strong forward scattering and significant near-field amplification occur.

Under these conditions, the scattering efficiency is governed by the following equation [34],

$$Q_{\text{sca}} = \frac{2}{x^2} \sum_{n=1}^{\infty} (2n+1) (|a_n|^2 + |b_n|^2), \quad (14)$$

where a_n and b_n are the electric and magnetic Mie coefficients, respectively. This equation governs that moderate x -values enhance multipolar resonance excitation while minimizing the reflected power. On the other hand, due to the negligible parasitic absorbance of SiO₂, it redistributes upcoming photons into the absorber region. This redistribution increases the local optical field intensity according to the equation,

$$p_{\text{abs}} = \frac{1}{2} \omega \epsilon_0 \text{Im}[\epsilon] |E|^2, \quad (15)$$

Figs. 4(c) and (d) represent the optical J_{sc} and percentage (%) improvement, J_{sc} and from these figures it is clearly seen that maximum J_{sc} is found in the configuration three for higher optical confinement in the nanostructure. Moreover, this improvement is supported by the generation profiles for these three configurations. According to Figs. 5(a)–(c), our proposed structure exhibits a higher optical (J_{sc}) of 29.53 mA/cm² and an enhanced generation rate ($1.56 \times 10^{28} \text{ m}^3/\text{s}$) across the absorber layer. The configuration with the SiO₂ sphere embedded inside the ITO layer shows the most efficient light trapping and photogeneration, confirming the effectiveness of this design in improving the performance of the device. The high generation rate is directly linked to the robust electric field confinement present in the active region, as demonstrated by the electric field profile detailed below.

Fig. 6 (a) illustrates the electric field distribution at a wavelength of 300 nm. The field profile exhibits significant

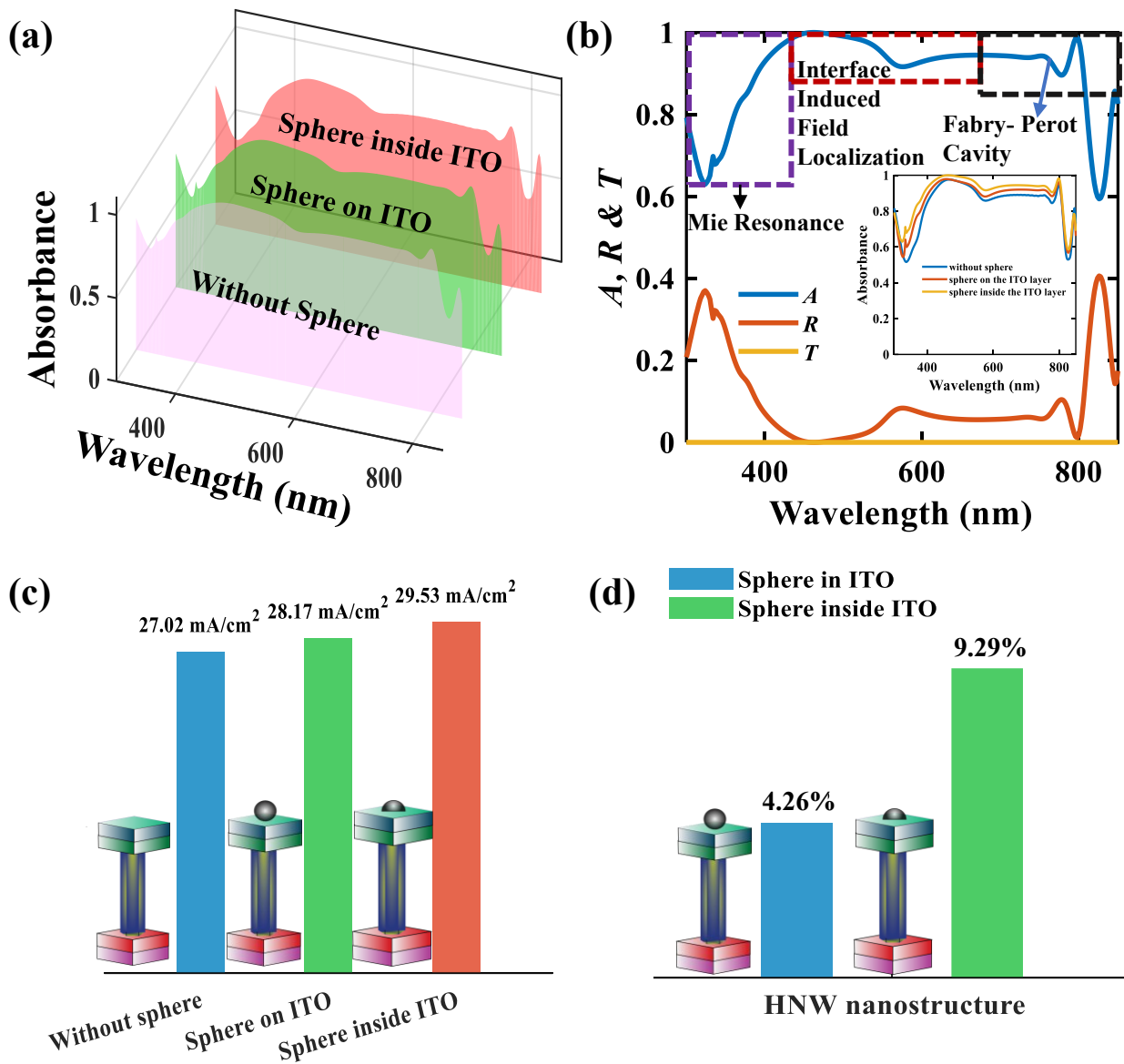


Figure 4: (a) Absorbance spectral density for three different configurations of the optimized structure. The inset shows the variation of absorbance spectra for the three configurations, (b) absorbance, reflectance, and transmittance spectra for the configuration of penetrating the sphere into the ITO layer, (c) J_{sc} values for these three different configurations (d) percentage (%) improvement in J_{sc} .

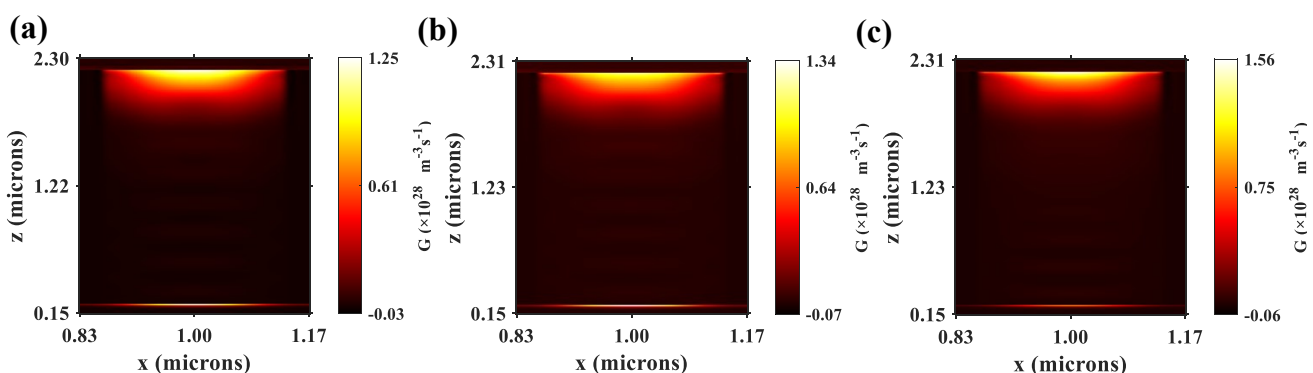


Figure 5: Generation profile for our proposed structure: (a) without sphere, (b) sphere on top of ITO layer, (c) sphere inside the ITO layer.

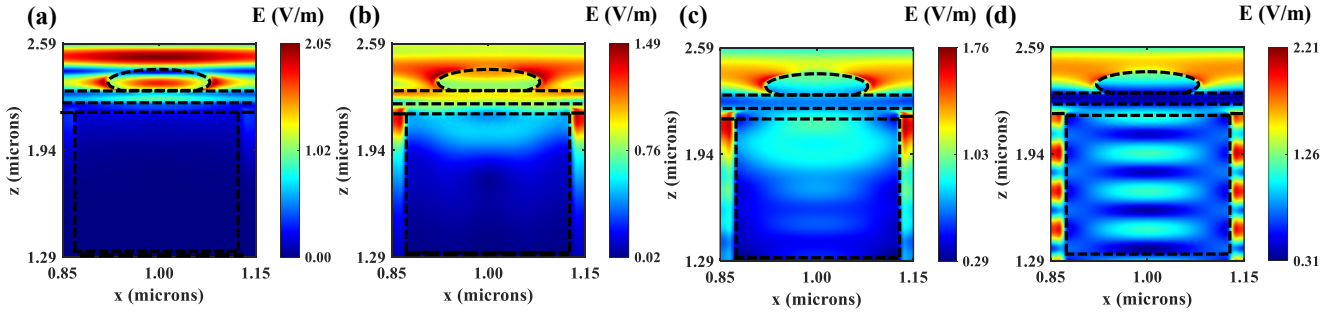


Figure 6: Electric field distribution at different wavelengths: (a) $\lambda = 300$ nm, (b) $\lambda = 430$ nm, (c) $\lambda = 762$ nm, and (d) $\lambda = 826$ nm for the structure with SiO_2 sphere inside the ITO layer.

confinement of the photon at the upper hemispherical section of the SiO_2 sphere, while minimal field penetration occurs into the perovskite layer. This phenomenon characterizes the high-order Mie resonance that arises from the refractive index difference between the SiO_2 sphere and its surrounding medium. Despite the strong intensity of the field at the sphere surface, the limited field localization into the perovskite layer leads to insufficient light harvesting at this wavelength due to the low optical penetration depth. In Fig. 6 (b), at a wavelength of 430 nm, the electric field starts to spread more effectively toward the lower half of the SiO_2 sphere and the upper part of the perovskite layer. This can be due to the interface-induced field confinement followed by low Fresnel reflection rather than any explicit resonant mode. Here, the SiO_2 sphere changes the direction of the incident plane waves into near-field energy. As a result, the HNW perovskite layer begins to support broadband absorption, which increases the intensity of the internal field. At 762 nm, as depicted in Fig. 6 (c), the electric field exhibits clear vertical guiding patterns within the HNW. This indicates the FP-cavity effect due to the internal reflectance and disperses the propagation of the localized field across the device due to the symmetry of the HNW. At 826 nm, as illustrated in Fig. 6 (d), a standing wave pattern has been observed throughout the HNW. On the other hand, the SiO_2 sphere acts as a passive coupling layer due to its lower refractive index compared to the surrounding materials at this wavelength regime.

Furthermore, to gain a better understanding of the carrier transport mechanisms in our proposed PSCs, the energy band alignment across the HTL to ETL is shown in Fig. 7. The conduction band (CB) and valence band (VB) levels of each layer are selected to facilitate efficient charge separation and directional transport. From the figure, it can be observed that there is a smooth transition of the charge carriers throughout the cell, indicating effective carrier transport throughout the device. This smooth band alignment across the interfaces minimizes potential barriers, suppressed recombination, and supports a strong built-in electric field. This plays a significant role in achieving high J_{sc} and V_{oc} , ultimately enhancing the overall PCE.

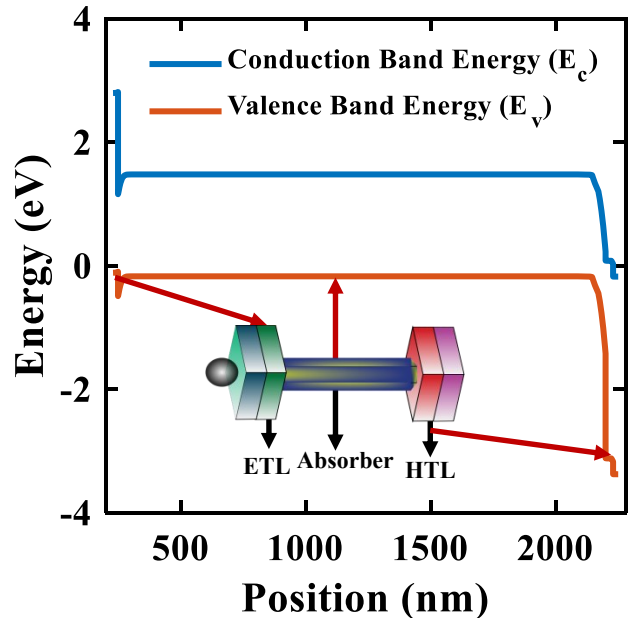


Figure 7: Band alignment across the layer of the optimized HNW PSC.

3.2. Impact of Light Polarization on Device Performance

To attain the outstanding PV performance, it is crucial to ensure polarization-independent absorbance capabilities across the entire wavelength range. This study examined both optical and electrical characteristics under polarized light illumination. Figs. 8 (a) and (b) represent the line and contour plots of the absorbance spectra corresponding to the presence of various polarization angles ranging from $\varphi = 0^\circ$ to $\varphi = 90^\circ$. The absorbance spectra exhibit negligible variation across varying polarization angles, consistently displaying high absorbance levels ($> 85\%$) throughout the wavelength range of 300–850 nm. This validates the spectral uniformity and indicates a stable absorbance band that remains largely unaffected by changes in polarization. Moreover, the average absorbance (A_{avg}) showed only a slight variation due to the variation in polarization angle from $\varphi = 0^\circ$ to $\varphi = 90^\circ$. The (A_{avg}) decreased from 89.86% to 85.83%, which denoted a relative change of 4.03%. In

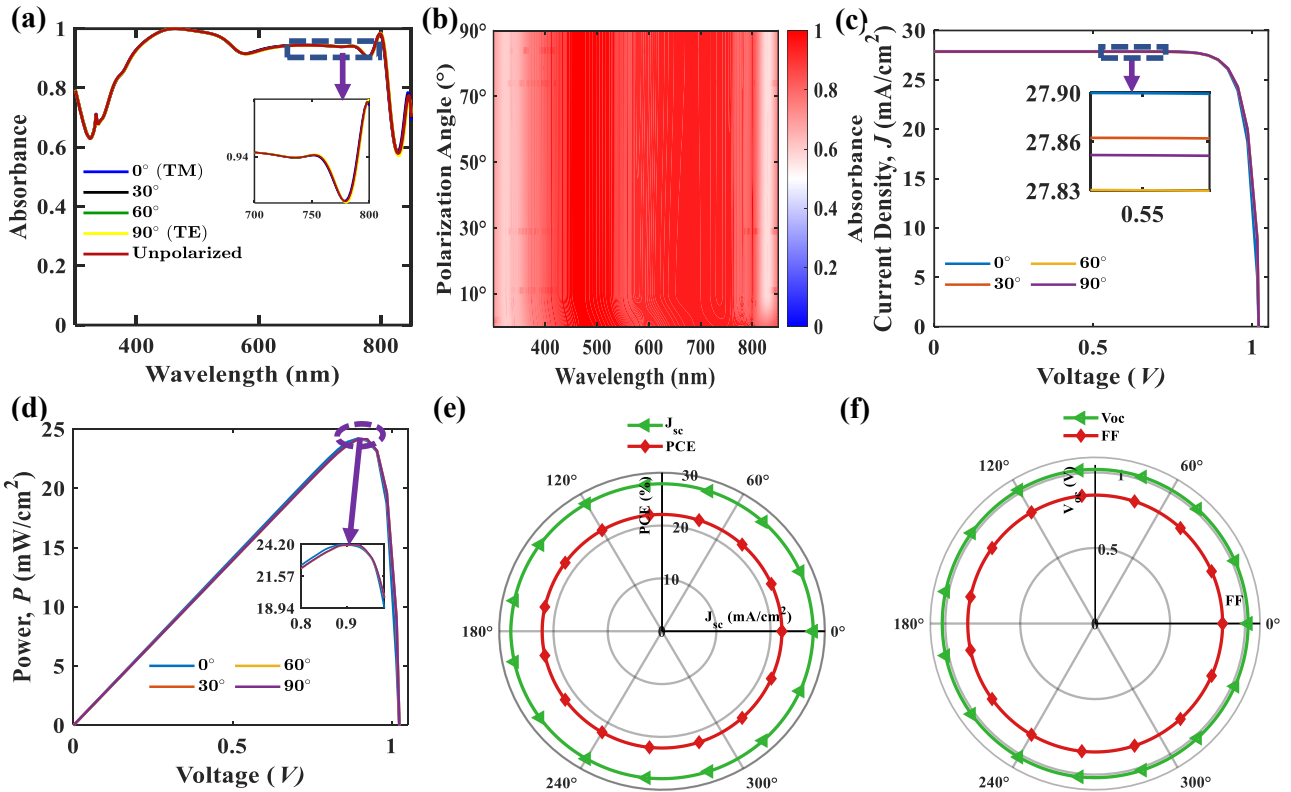


Figure 8: (a) Absorbance spectra for different polarization states and an unpolarized light source of the optimized structure, (b) color map of polarization angle-dependent absorbance spectra, (c) and (d) J - V and P - V curves for the proposed HNW PSC; the inset shows the zoom view of the J - V and P - V characteristics. Polar plots of (e) J_{sc} and PCE and (f) V_{oc} and FF for the proposed HNW PSC for $\varphi = 0^\circ$ to $\varphi = 360^\circ$.

addition, we evaluated the performance using the unpolarized light source, which is illustrated in Fig. 8 (a), where the consistency in spectral behavior confirms the isotropic interaction with light regardless of the polarization.

The electrical performance of the proposed HNW PSC was investigated by importing the generation rate profile extracted from the optical simulations into the solver to perform a self-consistent solution of Poisson's equation and the drift-diffusion equations for electrons and holes under AM 1.5G solar illumination (100 mW/cm 2). The electrical properties of the materials used in the simulation are given in Table 1 [35]. Fig. 8 (c) shows the simulated current density-voltage (J - V) curves across different polarization angles, ranging from 0° to 90°. The figure shows only minor changes, indicating that the HNW architecture preserves essentially stable charge-carrier dynamics regardless of polarization angles. Similarly, the corresponding power density-voltage (P - V) curves shown in Fig. 8 (d) further confirm that the device's consistent energy conversion behavior across the polarization states. The extracted values of J_{sc} , V_{oc} , fill factor (FF), and PCE at each polarization angle are summarized in Table 2. As observed, all key figures of merit remain stable, with no meaningful performance loss across the polarization angles. This behavior is primarily attributed to the geometric symmetry of the HNW and its isotropic light coupling, which together yield a uniform

Table 2

Electrical performance parameters of the proposed PSC as a function of polarization angles (φ) ranging from 0° to 90°

φ	J_{sc} (mA/cm 2)	PCE (%)	V_{oc} (V)	FF
0°	27.90	24.2	1.02	0.85
30°	27.86	24.15	1.02	0.85
60°	27.83	24.13	1.02	0.85
90°	27.87	24.16	1.02	0.85

optical and electrical response regardless of the incident light's polarization. Figs. 8 (e) and (f) demonstrate the PV performance parameters as a function of polarization angle varied from $\varphi = 0^\circ$ to $\varphi = 360^\circ$. Both figures exhibit flawless circular and symmetrical distributions over the full cycle rotation. The absence of significant angular modulation indicates that the generated photocurrent and the carrier transport mechanisms are not perturbed by the polarization-dependent effects, underscoring the intrinsic isotropy of the HNW structure.

3.3. Impact of Incident Angle on Device Performance

To evaluate the angular dependency of the proposed HNW PSC, both optical and electrical simulations were

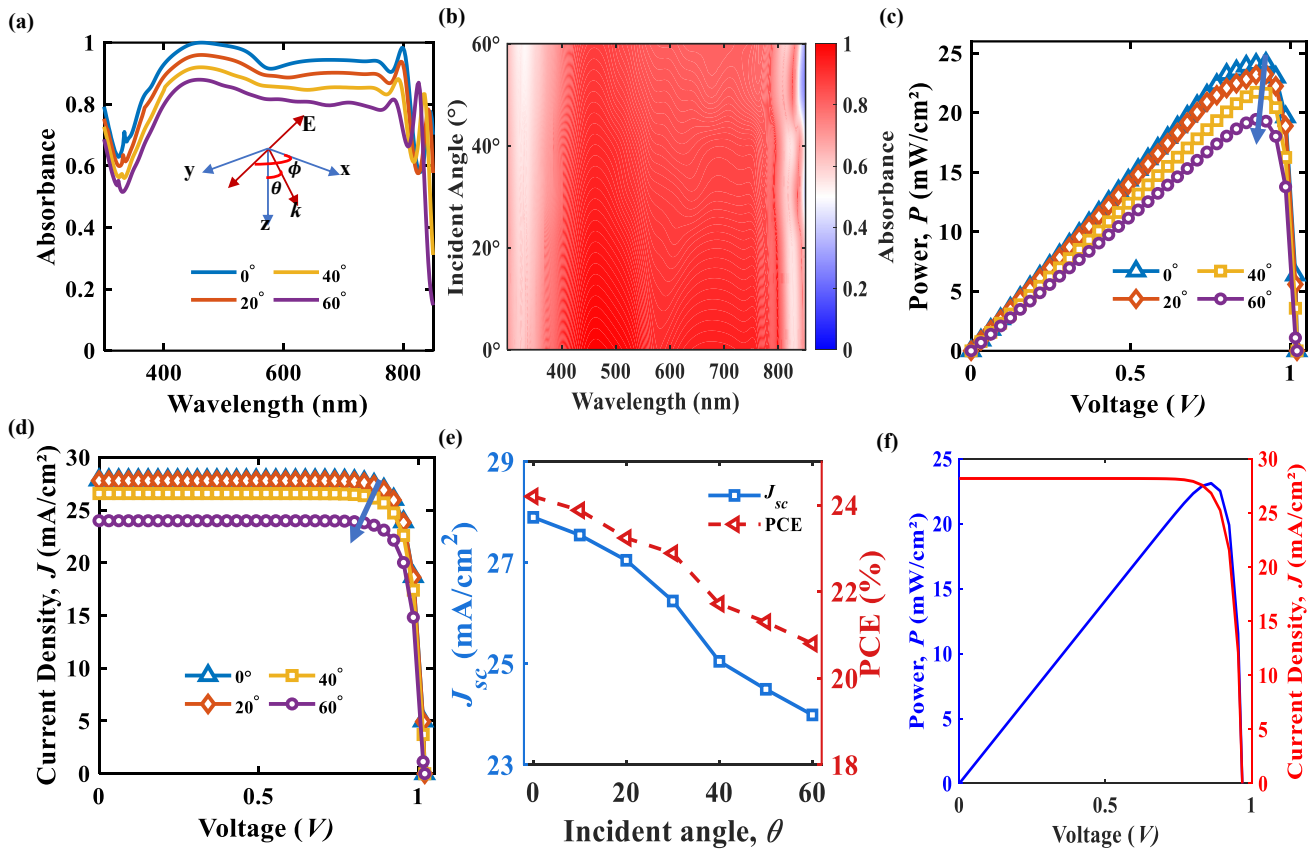


Figure 9: (a) and (b) Absorbance spectra at $\theta = 0^\circ$ to $\theta = 60^\circ$; the inset shows the polarization angle, φ , and the incident angle, θ of the plane wave, (c) and (d) $P - V$ and $J - V$ curve for unpolarized incident light at $\theta = 0^\circ$ to $\theta = 60^\circ$ for the proposed structure, (e) comparison of electrical parameters (J_{sc} , PCE) under unpolarized incident light at $\theta = 0^\circ$ to $\theta = 60^\circ$, and (f) $J - V$ and $P - V$ for the proposed HNW PSC at normal incident light for unpolarized light source.

conducted under oblique illumination of the unpolarized incident light source. The angle of incidence (θ) of unpolarized light was systematically varied from 0° to 60° , while all structural and material parameters were kept unchanged. Figs. 9 (a) and (b) illustrate the absorbance spectra in both line and contour formats for different θ values. The device exhibits a broad and spectrally stable absorbance profile throughout the visible range, indicating that the HNW architecture effectively preserves optical resonances under oblique illumination. However, a gradual reduction in absorbance intensity is observed with increasing θ , which can be attributed to the reduced effective optical path length and weaker coupling of incident photons within the proposed structure.

The A_{avg} decreases from 89.82% at normal incidence to 77.27% at $\theta = 60^\circ$, corresponding to a relative reduction of only 12.55%. The influence of θ on electrical performance is shown in Figs. 9(c) and (d) through the J - V and P - V characteristics. As θ increases, both the J_{sc} and maximum output power (P_{max}) decrease in accordance with the reduced optical absorbance. Under normal incidence, J_{sc} and P_{max} reach values of 27.85 mA/cm² and 24.17 mW/cm², respectively. At $\theta = 20^\circ$, the average absorbance decreases, resulting in J_{sc} and P_{max} of 27.04 mA/cm² and 23.24

Table 3

Electrical performance parameters of our proposed PSC for different incident angles θ ranging from 0° to 60°

θ	J_{sc} (mA/cm ²)	PCE (%)	V_{oc} (V)	FF
0°	27.85	24.15	1.02	0.85
20°	27.04	23.44	1.02	0.85
40°	25.05	21.72	1.02	0.85
60°	23.99	20.8	1.02	0.85

mW/cm², respectively, corresponding to a relative change of 2.9% and 3.97% compared to the normal incidence. Over the full angular range from 0° to 60° , the proposed structure maintains a J_{sc} of 27.85 and 23.99 mA cm⁻² while the V_{oc} and FF remain nearly constant, indicating robust carrier transport characteristics. Fig. 9 (e) compares the variation of J_{sc} and PCE as a function of θ . The detailed PV parameters are summarized in Table 3. The resulting J - V and P - V characteristics under the normal incidence of unpolarized light are presented in Fig. 9 (f), demonstrating strong current generation and high power output.

3.4. Proposed Cell Fabrication Method

The device can be fabricated on cleaned glass substrates, where Al back electrodes can be thermally deposited in a high-vacuum environment to form the reflective bottom contact, following the typical approach for n-i-p PSCs [36]. After that, an HTL layer made of spiro-OMeTAD can be deposited via spin coating from a chlorobenzene solution containing Li-trifluoromethanesulfonylimide (TFSI) and tert-butylpyridine (tBP), followed by controlled drying under low-humidity conditions to promote oxidation and increase conductivity [37]. The HNW-based absorber layer made of MAPbI₃, which is intended to be fabricated utilizing an anodic aluminum oxide (AAO) template that inherently retains a self-structured hexagonal pore design generated during the electrochemical anodization of Al under fixed voltage and electrolyte conditions, and is laminated onto the spiro-OMeTAD/Al layer [38]. The PbI₂ precursor solution can be infiltrated into the template's pores and converted to CH₃NH₃PbI₃ by immersing it in methylammonium iodide, followed by an annealing process. To achieve the desired heights of the NW, multiple infiltration-conversion cycles may be employed, followed by a partial removal of the template using dilute H₃PO₄ to reveal the wire tips while preserving the voids between the wires [39]. To mitigate parasitic absorbance and moisture penetration in these void areas, insulating fillers like Polymethyl methacrylate (PMMA) can be added through spin coating from an anisole solution, due to its optical transparency ($k \approx 0$ in the visible spectrum), moderate refractive index ($n \approx 1.48$), and proven compatibility with perovskite devices [40]. In addition, low-refractive-index materials like CYTOP fluoropolymer ($n \approx 1.34$) or MgF₂ ($n \approx 1.38$) can also be employed to infill the cavities while introducing negligible optical loss [41]. After infilling, the NW sidewalls will undergo a short treatment with phenethylammonium iodide (PEAI) to passivate interfacial defects and enhance carrier lifetime [42]. A compact ETL of TiO₂ will then be deposited through atomic layer deposition to guarantee close contact with the perovskite NW and facilitate efficient electron extraction [42]. The final step involves forming a transparent conducting electrode by RF sputtering of ITO, thereby completing the vertical charge transport pathway. In order to enhance optical scattering and near field confinement, SiO₂ nanospheres synthesized via the Stöber method can be applied to the ITO using spin coating, followed by partial embedding through the deposition of an additional thin ITO layer. The hemispherical SiO₂ structures are anticipated to function as photonic scatterers to improve light coupling, aligning with prior strategies in nanophotonic light management for thin-film PVs [43].

4. Comparative Analysis

Table 4 demonstrates the comparative analysis of the PV performance of our proposed HNW PSC with the previously reported works. Fu *et al.* presented a cylindrical MAPbI₃ microstructured cell that demonstrated improved optical confinement and achieved a PCE of about 20.19%,

with an average absorbance exceeding 90% in the visible region, attributed to enhanced light absorbance facilitated by the microcavity design. Similarly, Joyti *et al.* reported a 3D/3D MAPbI₃/FAPbI₃ bilayer heterojunction that achieved an efficiency greater than 23% while also showing enhanced device stability. In another study, Noori *et al.* introduced a MAPbI₃/CsPbI₃ heterojunction that achieved a PCE of 20.5%, emphasizing the important role of band alignment in efficient charge separation and transport. Though the above-mentioned works mainly focused on optical confinement, some researchers placed their interest on modifications to the transport layer. Jing *et al.* reported Sb₂Se₃ as a narrow-bandgap HTL, improving hole mobility and reducing recombination losses, while Li *et al.* conducted simulations on SnS₂/MoS₂-based ETL and HTL combinations to balance charge extraction. Likewise, Son *et al.* further optimized the internal device parameters and reached an efficiency of 19.3%, even if their planar structure was limited by optical path length and trapping capabilities. Notably, all the above studies are essentially focused on improving either optical absorbance or charge transport processes. However, few studies have incorporated both of these aspects into a single design.

On the other hand, the HNW structure presented in this study incorporates both geometric light management and electrical optimization, resulting in a theoretical PCE of 24.2% that outperforms all the above-mentioned studies. The NW geometries open up a new room for enhanced photon management and carrier transport. This improvement is due to the combined effects of Mie and FP-cavity while maintaining polarization robustness under TE, TM, and unpolarized illumination. Overall, the result highlights the advantage of structural photonic design over conventional planar or bilayer configurations.

5. Conclusion

In this paper, we meticulously designed an ingenious HNW PSC structure and systematically elucidated the optoelectrical performance by integrating electromagnetic field analysis with carrier dynamics governed by the Poisson and drift-diffusion equations. In contrast to planar or cylindrical nanostructures, the rotational symmetry offered by the HNW structure enables broadband absorption in both TE and TM polarizations, ensuring polarization-independent absorbance across the entire wavelength spectrum. By partially inserting a dielectric SiO₂ sphere into the ITO layer, the design effectively utilized both Mie resonance and FP-cavity, which also enhanced near-field confinement, resulting in more efficient electron-hole generation near the active region. Detailed optical simulations showed that the proposed design greatly reduced reflectance and transmittance losses. Electrical simulations confirmed these improvements, yielding a high PCE of 24.2% with corresponding FF and V_{oc} of 0.85 and 1.02 V, respectively, under AM 1.5G solar illumination. Besides the quantitative results, this study highlights the important relationship among nanoscale

Table 4
Comparison of performances among our work and previously reported works

Structure	Active Layer	J_{sc} (mA cm $^{-2}$)	V_{oc} (V)	FF	PCE (%)	Ref.
HNW	$\text{CH}_3\text{NH}_3\text{PbI}_3$	27.90	1.02	0.85	24.2	This work
Inverted Pyramid	$\text{CH}_3\text{NH}_3\text{PbI}_3$	27.81	0.95	0.82	21.85	[44]
Cylindrical	$\text{CH}_3\text{NH}_3\text{PbI}_3$	24.50	0.97	-	20.19	[45]
Planar	$\text{CH}_3\text{NH}_3\text{PbI}_3/\text{FAPbI}_3$	25.00	1.16	0.79	23.08	[46]
Planar	$\text{CH}_3\text{NH}_3\text{PbI}_3/\text{CSPbI}_3$	24.66	1.06	0.78	20.5	[47]
Planar	$\text{CH}_3\text{NH}_3\text{PbI}_3$	43.03	0.65	0.785	21.90	[48]
Planar	$\text{CH}_3\text{NH}_3\text{PbI}_3$	24.91	0.97	0.74	19.30	[49]
Planar	$\text{CH}_3\text{NH}_3\text{PbI}_3$	25.72	0.84	0.78	16.95	[50]

geometry, light-matter interactions, and carrier dynamics. Ultimately, this study demonstrates that combining photonic confinement with electronic transport in the HNW geometry can enable the development of innovative, highly efficient PSCs using scalable and flexible design strategies.

CRediT authorship contribution statement

Kawshik Nath: Conceptualization, Methodology, Visualization, Software, Investigation, Writing – original draft. **Bibekananda Nath:** Conceptualization of this study, Methodology, Software. **Ahmed Zubair:** Conceptualization of this study, Methodology, Software.

Data Availability Statement

The data supporting the findings presented in this paper are not currently available to the public, but they may be obtained from the authors upon reasonable request.

Acknowledgements

The authors thank the Bangladesh University of Engineering and Technology (BUET) for providing technical support.

References

- [1] Bingquan Liang, Xinliang Chen, Xiaofeng Wang, Heze Yuan, Aixin Sun, Zheng Wang, Liyuan Hu, Guofu Hou, Ying Zhao, and Xiaodan Zhang. Progress in crystalline silicon heterojunction solar cells. *Journal of Materials Chemistry A*, 13:2441–2477, 2025.
- [2] Md. Faiaad Rahman, Md. Ashaduzzaman Niloy, Ehsanur Rahman, and Ahmed Zubair. Unveiling architectural and optoelectronic synergies in lead-free perovskite/perovskite/kesterite triple-junction monolithic tandem solar cells. 2025.
- [3] Nowshin Akhtary and Ahmed Zubair. Light trapping using a dimer of spherical nanoparticles based on titanium nitride for plasmonic solar cells. *Optical Materials Express*, 13(10):2759–2774, Oct 2023.
- [4] Partha Pratim Nakti, Dip Sarker, Md Ishfak Tahmid, and Ahmed Zubair. Ultra-broadband near-perfect metamaterial absorber for photovoltaic applications. *Nanoscale Advances*, 5:6858–6869, 2023.
- [5] Jiye Han, Keonwoo Park, Shaun Tan, Yana Vaynzof, Jingjing Xue, Eric Wei-Guang Diau, Mounji G. Bawendi, Jin-Wook Lee, and Il Jeon. Perovskite solar cells. *Nature Reviews Methods Primers*, 5(1):3, Jan 2025.
- [6] Rahul Pandey, Sagar Bhattacharai, Kulbhushan Sharma, Jaya Madan, Ali K Al-Mousoi, Mustafa KA Mohammed, and M Khalid Hossain. Halide composition engineered a non-toxic perovskite–silicon tandem solar cell with 30.7% conversion efficiency. *ACS Applied Electronic Materials*, 5(10):5303–5315, 2023.
- [7] Ali K Al-Mousoi, Mustafa KA Mohammed, Anjan Kumar, Rahul Pandey, Jaya Madan, Davoud Dastan, M Khalid Hossain, P Sakthivel, Zaher Mundher Yaseen, et al. Understanding auger recombination in perovskite solar cells. *Physical Chemistry Chemical Physics*, 25(24):16459–16468, 2023.
- [8] Akihiro Kojima, Kenjiro Teshima, Yasuo Shirai, and Tsutomu Miyasaka. Organometal halide perovskites as visible-light sensitizers for photovoltaic cells. *Journal of the American Chemical Society*, 131(17):6050–6051, 2009.
- [9] Shuyan Shao, Jian Liu, Giuseppe Portale, Hong-Hua Fang, Graeme R Blake, Gert H ten Brink, L Jan Anton Koster, and Maria Antonietta Loi. Highly reproducible Sn-based hybrid perovskite solar cells with 9% efficiency. *Advanced Energy Materials*, 8(4):1702019, 2018.
- [10] Harshit Sharma, Vinay K. Verma, Ram Chandra Singh, Pramod K. Singh, and Arindam Basak. Numerical analysis of high-efficiency $\text{CH}_3\text{NH}_3\text{PbI}_3$ perovskite solar cell with PEDOT:PSS hole transport material using SCAPS 1D simulator. *Journal of Electronic Materials*, 52(7):4338–4350, Jul 2023.
- [11] Md. Faiaad Rahman, Arpan Sur, and Ahmed Zubair. Hierarchically structured, high-efficiency and thermally robust perovskite solar cells with band-engineered double-hole layers. *Solar Energy Materials and Solar Cells*, 2026.
- [12] Nam Joong Jeon, Hyejin Na, Eui Hyuk Jung, Tae-Youl Yang, Yong Guk Lee, Geunjin Kim, Hee-Won Shin, Sang Il Seok, Jaemin Lee, and Jangwon Seo. A fluorene-terminated hole-transporting material for highly efficient and stable perovskite solar cells. *Nature Energy*, 3(8):682–689, 2018.
- [13] Wolfgang Tress, Nevena Marinova, Olle Inganäs, Mohammad K Nazeeruddin, Shaik M Zakeeruddin, and Michael Graetzel. Predicting the open-circuit voltage of $\text{CH}_3\text{NH}_3\text{PbI}_3$ perovskite solar cells using electroluminescence and photovoltaic quantum efficiency spectra: the role of radiative and non-radiative recombination. *Advanced Energy Materials*, 5(3):1400812, 2015.
- [14] Uwe Rau, Beatrix Blank, Thomas CM Müller, and Thomas Kirchartz. Efficiency potential of photovoltaic materials and devices unveiled by detailed-balance analysis. *Physical Review Applied*, 7(4):044016, 2017.
- [15] Juan-Pablo Correa-Baena, Michael Saliba, Tonio Buonassisi, Michael Grätzel, Antonio Abate, Wolfgang Tress, and Anders Hagfeldt. Promises and challenges of perovskite solar cells. *Science*, 358(6364):739–744, 2017.
- [16] Harshit Sharma, Vinay K Verma, Ram Chandra Singh, Pramod K Singh, and Arindam Basak. Numerical analysis of high-efficiency $\text{CH}_3\text{NH}_3\text{PbI}_3$ perovskite solar cell with PEDOT:PSS hole transport material using SCAPS-1D simulator. *Journal of Electronic Materials*, 52(7):4338–4350, 2023.

[17] Yahong Wang, Yunfei He, Yin Ren, Sisi Li, Lin He, Peng Ye, Luming Zhou, Zhenhua Wang, Rongli Gao, Wei Cai, et al. Effects of complexing agent on carrier transport property and photovoltaic performance of TiO_2 @ MAPbI_3 core-shell structured nanowire arrays. *Solar Energy Materials and Solar Cells*, 271:112868, 2024.

[18] Ghofrane Hmaidi and Hassen Derouiche. PEDOT: PSS as hole-selective layer on hybrid solar cells. *Materials Research Innovations*, pages 1–7, 2025.

[19] Yin Ren, Yunfei He, Sisi Li, Yahong Wang, Lin He, Peng Ye, Luming Zhou, Rongli Gao, Gang Chen, Wei Cai, et al. A new type of core-shell nanowire array structured quantum dot-composite perovskite solar cell with near full-spectrum absorption. *Physica E: Low-dimensional Systems and Nanostructures*, 160:115937, 2024.

[20] Xinlei Wang and Bingqiang Cao. Efficient perovskite solar cells with tunable transmittance using transparent conductive silver nanowire network electrodes. *Applied Physics A*, 131(6):432, 2025.

[21] Jieyang Liang, Yanan Wang, Yufeng Zhang, Xiaolin Liu, and Jia Lin. Construction of perovskite homojunction for highly efficient perovskite solar cells by SCAPS-1D. *Materials Science and Engineering: B*, 301:117196, 2024.

[22] Hussain J Alathlawi, Selma Rabhi, Tarak Hidouri, Hind Adawi, Fadiyah A Makin, and Amani A Alsam. Role of Ag nanowires: Mnexes in optimizing flexible, semitransparent bifacial inverted perovskite solar cells for Building-Integrated Photovoltaics: A SCAPS-1D modeling approach. *Advanced Theory and Simulations*, 8(3):2401004, 2025.

[23] EM Mkawi, Saif MH Qaid, Iman S Roqan, Y Al-Hadeethi, FG Almehmadi, Hadeel A Alamoudi, Fatimah Alreshidi, Sanad A Alsulaiman, Hassan I Jaafari, Yahya Alajlani, et al. Enhancement the performance of MAPbI_3 perovskite solar cells via germanium sulfide doping. *Optical Materials*, 157:116089, 2024.

[24] Jyoti V Patil, Sawanta S Mali, and Chang Kook Hong. Exceeding 23% efficiency for 3d/3d bilayer perovskite heterojunction MAPbI_3 / FAPbI_3 -based hybrid perovskite solar cells with enhanced stability. *Advanced Functional Materials*, 35(1):2408721, 2025.

[25] Jeong-Hyeok Im, Jingshan Luo, Marius Franckevicius, Norman Pellet, Peng Gao, Thomas Moehl, Shaik Mohammed Zakeeruddin, Mohammad Khaja Nazeeruddin, Michael Gratzel, and Nam-Gyu Park. Nanowire perovskite solar cell. *Nano letters*, 15(3):2120–2126, 2015.

[26] Ranbir Singh, Sanjaykumar R Suranagi, Seok Joo Yang, and Kilwon Cho. Enhancing the power conversion efficiency of perovskite solar cells via the controlled growth of perovskite nanowires. *Nano Energy*, 51:192–198, 2018.

[27] Jeongbeom Cha, Mi Kyong Kim, Wonjong Lee, Haedam Jin, Hyemi Na, Dinh Cung Tien Nguyen, Soo-Hyoung Lee, Jongchul Lim, and Min Kim. Perovskite nanowires as defect passivators and charge transport networks for efficient and stable perovskite solar cells. *Chemical Engineering Journal*, 451:138920, 2023.

[28] Bibekananda Nath and Ahmed Zubair. Broadband high-temperature multilayer pyramid-shaped metamaterial thermal absorber for thermophotovoltaic applications. *Case Studies in Thermal Engineering*, 78:107697, 2026.

[29] ANSYS, Inc. *Ansys Lumerical: 3D Electromagnetic Simulator, Release 2024 R1*. ANSYS, Inc., 2024.

[30] Edward D Palik. *Handbook of optical constants of solids*, volume 3. Academic press, 1998.

[31] Shorok Elewa, Bedir Yousif, and Mohy Eldin A. Abo-Elsoud. Improving efficiency of perovskite solar cell using optimized front surface nanospheres grating. *Applied Physics A*, 127(11):854, Oct 2021.

[32] Qi Luo, Xueshuang Deng, Chenxi Zhang, Meidong Yu, Xin Zhou, Zengbo Wang, Xiaohong Chen, and Sumei Huang. Enhancing photovoltaic performance of perovskite solar cells with silica nanosphere antireflection coatings. *Solar Energy*, 169:128–135, 2018.

[33] Craig F Bohren and Donald R Huffman. *Absorption and scattering of light by small particles*. John Wiley & Sons, 2008.

[34] Lukas Novotny and Bert Hecht. *Principles of nano-optics*. Cambridge university press, 2012.

[35] Afsaneh Asgariyan Tabrizi, Hamed Saghaei, Mohammad Amin Mehranpour, and Mehdi Jahangiri. Enhancement of absorption and effectiveness of a perovskite thin-film solar cell embedded with gold nanospheres. *Plasmonics*, 16(3):747–760, Jun 2021.

[36] Julian Burschka, Norman Pellet, Soo-Jin Moon, Robin Humphry-Baker, Peng Gao, Mohammad K. Nazeeruddin, and Michael Grätzel. Sequential deposition as a route to high-performance perovskite-sensitized solar cells. *Nature*, 499(7458):316–319, Jul 2013.

[37] Nam Joong Jeon, Jun Hong Noh, Young Chan Kim, Woon Seok Yang, Seungchan Ryu, and Sang Il Seok. Solvent engineering for high-performance inorganic–organic hybrid perovskite solar cells. *Nature Materials*, 13(9):897–903, Sep 2014.

[38] Qiaoling Xu and Guowen Meng. *Porous Anodic Aluminum Oxide*. Springer Berlin Heidelberg, Berlin, Heidelberg, 2013.

[39] Tong Zhou, Hongtao Lai, Tingting Liu, Di Lu, Xiangjian Wan, Xiaodan Zhang, Yongsheng Liu, and Yongsheng Chen. Highly efficient and stable solar cells based on crystalline oriented 2D/3D hybrid perovskite. *Advanced Materials*, 31(32):e1901242, June 2019.

[40] Nakita K. Noel, Samuel D. Stranks, Antonio Abate, Christian Wehrenfennig, Simone Guarnera, Amir-Abbas Haghhighirad, Aditya Sadhanala, Giles E. Eperon, Sandeep K. Pathak, Michael B. Johnston, Annamaria Petrozza, Laura M. Herz, and Henry J. Snaith. Lead-free organic–inorganic tin halide perovskites for photovoltaic applications. *Energy & Environmental Science*, 7:3061–3068, 2014.

[41] Mark L. Brongersma, Yi Cui, and Shanhai Fan. Light management for photovoltaics using high-index nanostructures. *Nature Materials*, 13(5):451–460, May 2014.

[42] Woon Seok Yang, Jun Hong Noh, Nam Joong Jeon, Young Chan Kim, Seungchan Ryu, Jangwon Seo, and Sang Il Seok. SOLAR CELLS. high-performance photovoltaic perovskite layers fabricated through intramolecular exchange. *Science*, 348(6240):1234–1237, June 2015.

[43] K. R. Catchpole and A. Polman. Design principles for particle plasmon enhanced solar cells. *Applied Physics Letters*, 93(19):191113, 11 2008.

[44] Design and analysis of high-efficiency perovskite solar cell using the controllable photonic structure and plasmonic nanoparticles. *Journal of Alloys and Compounds*, 960:170994, 2023.

[45] Wenfeng Fu, Chong Pan, Aixuan Zhou, Pengcheng Shi, Zao Yi, and Qingdong Zeng. Light absorption-enhanced ultra-thin perovskite solar cell based on cylindrical MAPbI_3 microstructure. *Materials*, 17(24), 2024.

[46] Jyoti V. Patil, Sawanta S. Mali, and Chang Kook Hong. Exceeding 23% efficiency for 3d/3d bilayer perovskite heterojunction MAPbI_3 / FAPbI_3 -based hybrid perovskite solar cells with enhanced stability. *Advanced Functional Materials*, 35(1):2408721, 2025.

[47] Darko Abdalla Noori. Heterojunction active layer MAPbI_3 / CsPbI_3 design for high-performance perovskite solar cells: a computational analysis achieving 20.5% efficiency. *Journal of Computational Electronics*, 24(2):43, Feb 2025.

[48] Jing Wu, Zhengyang Zhao, Zimeng Zhao, Min Zhang, Yuying Bi, Xibin Li, and Linrui Zhang. Simulation analysis of Sb_2Se_3 narrow bandgap hole transport layer in MAPbI_3 perovskite solar cells. *Journal of Electronic Materials*, 54(5):3910–3923, May 2025.

[49] Chaerin Son, Hyojung Son, and Byoung-Seong Jeong. Enhanced conversion efficiency in MAPbI_3 perovskite solar cells through parameters optimization via SCAPS-1D simulation. *Applied Sciences*, 14(6), 2024.

[50] Min Li, Shuai Guo, Xiaoyu Zhao, Sufeng Quan, Xuefeng Wang, Mengxuan Wu, Ruibin Liu, and Dieter Weller. Modeling and simulation of MAPbI_3 -based solar cells with SnS_2 as the electron transport layer (etl) and MoS_2 as the hole transport layer (HTL). *ACS Applied Electronic Materials*, 6(8):5997–6004, Aug 2024.